Improved Performance and Voltage Stability of Islanded Inverters Using Single-Loop PI-Lead Controller

Benzoubir, Mohammed E.; Lashab, Abderezak; Rayane, Khaled; Benmiloud, Mohammed; Bougrine, Mohamed; Benalia, Atallah; Trabelsi, Mohamed; Vahedi, Hani

DOI
10.1109/ACCESS.2025.3537716

Publication date
2025

Document Version
Final published version

Published in
IEEE Access

IEEE Access
Multidisciplinary ⋮ Rapid Review ⋮ Open Access Journal

Received 13 December 2024, accepted 30 January 2025, date of publication 3 February 2025, date of current version 6 February 2025.

Digital Object Identifier 10.1109/ACCESS.2025.3537716

RESEARCH ARTICLE

Improved Performance and Voltage Stability of Islanded Inverters Using Single-Loop PI-Lead Controller

MOHAMMED E. BENZOUBIR[1], ABDEREZAK LASHAB[2], (Senior Member, IEEE), KHALED RAYANE[1], MOHAMMED BENMILOUD[1], (Member, IEEE), MOHAMED BOUGRINE[1], ATALLAH BENALIA[1], MOHAMED TRABELSI[3], (Senior Member, IEEE), AND HANI VAHEDI[4], (Senior Member, IEEE)

[1]LACoSERE Laboratory, Electrical Engineering Department, University of Amar Telidji, Laghouat 03000, Algeria
[2]Center for Research on Microgrids (CROM), Aalborg University, 9220 Aalborg, Denmark
[3]Electronics and Communications Engineering Department, Kuwait College of Science and Technology, Kuwait City 27235, Kuwait
[4]Department of Electrical Engineering, Mathematics, and Computer Science, Delft University of Technology, 2628 CD Delft, The Netherlands

Corresponding author: Mohammed E. Benzoubir (m.benzoubir@lagh-univ.dz)

The project was funded by the Kuwait Foundation for the Advancement of Sciences (KFAS) under project code CN23-13EE-1882.

ABSTRACT This paper introduces a novel single-loop control scheme for voltage regulation in islanded inverters, using a proportional-integral-lead (PI-Lead) controller designed within the synchronous reference frame (SRF) through a loop-shaping approach. Commonly, dual-loop controllers have been employed for this purpose owing to several limitations, such as insufficient stability with a narrow gain margin, a trade-off between stability and bandwidth, and constrained bandwidth due to the need for a significantly lower outer voltage loop bandwidth compared to the inner current one. The proposed method overcomes these challenges by integrating a Lead compensator, which enhances voltage regulation by eliminating steady-state error, improving stability margins, and providing a fast transient response while maintaining robustness against model parameter variations. Additionally, the control strategy reduces dependence on current measurements, except when dealing with inductive loads where virtual resistor-based active damping is necessary. Despite the challenges posed by multi-resonance phenomena and coupling effects inherent in single-loop SRF-based modeling, a comprehensive frequency-domain analysis is performed, with systematic controller parameter design guidelines to mitigate multi-gain crossover issues. Rigorous experimental results validate the theoretical findings and simulations, demonstrating the superior performance and practical effectiveness of the proposed control strategy compared to existing methods.

INDEX TERMS Voltage source inverter, single-loop voltage control, PI-lead compensator, islanded mode, multi-gain crossover frequencies.

I. INTRODUCTION

Voltage source inverters (VSIs) constitute indispensable elements in modern power systems and play a pivotal role in enabling the seamless integration and management of distributed generators (DGs) [1]. These inverters serve the critical function of converting direct current (DC) power extracted from renewable sources, such as solar and wind, into alternating current (AC) electricity compatible with the grid, thereby ensuring the efficient and dependable transfer of energy [2]. Notably, grid-forming control is adopted for the control of VSIs, provide them with the unique ability to operate in both grid-connected and islanded modes [3]. This distinctive characteristic renders them particularly compelling for the development of microgrids, as it affords these systems the flexibility to transition

The associate editor coordinating the review of this manuscript and approving it for publication was Ujjwol Tamrakar.

smoothly between modes [4]. Consequently, microgrids can adeptly alternate between modes to fulfill diverse objectives, whether supporting weak grids by regulating voltage and frequency within acceptable parameters in the connected mode, or autonomously powering local loads and isolated regions in the islanded mode [4], [5].

To effectively leverage these advantages, it is imperative to implement high-performance control strategies [6]. These strategies should ensure that the output frequency and voltage amplitude of the converter system track the desired references, exhibiting both typical transient and steady-state performances. A wide array of control methodologies designed to meet these objectives have been extensively documented in the academic literature, including methods based on PI and P+R controllers [5], [7], [8], [9], sliding mode control [10], [11], robust H_2/H_∞ control [12], virtual oscillator control [13], [14], [15], model predictive control [16], [17], [18], and adaptive control [19], [20].

VSI control schemes are broadly classified into two categories: cascaded dual-loop current-voltage control and single-loop voltage control. Within the cascaded control framework which is the most popular, the approach entails a sequential regulation process for both capacitor voltage and inductor current across the LC filter connected to the VSI [21]. This process is bifurcated into two stages, where the initial stage focuses on current control through an inner loop, while the outer loop oversees the voltage regulation [22]. In this scheme, the inner loop functions as a virtual impedance in series with the LC filter's inductor, enhancing active damping and reducing the filter resonance [23], [24]. However, inherent digital control delays in this scheme may impair voltage control performance and risk system instability [21], [23], [25]. Moreover, this approach constrains the control dynamics, as the bandwidth of the inner current loop is required to be significantly higher — by a factor of four to ten times — than that of the voltage loop. Consequently, the bandwidth of the outer voltage loop is restricted to a few hundred Hertz [21], [23], [26].

On the contrary, the single-loop control scheme primarily focuses on the regulation of capacitor voltage through measurement and feedback, bypassing the need for high-resolution current sensors [27]. This scheme represents the most straightforward methodology for achieving regulation of the inverter's output voltage while maintaining zero steady-state error and fast transient response. Reference [28] presents a single-loop control strategy that incorporates a posicast controller to attenuate resonance effects. Nonetheless, the efficacy of the posicast controller is notably sensitive to the resonance frequency of the LC filter [29]. In [30] and [31], a method of direct pole placement, exploiting the discrete z-domain model of VSIs, is introduced as a solution to mitigate the resonance impact of the LC filter. However, this strategy introduces sensitivity to variations in system parameters [21]. [29], [31], [32] have demonstrated that controllers based on PI or PR mechanisms are challenged by instability issues. This instability arises as the proportional gain enhances system performance at the expense of phase margin reduction. Consequently, in [31] and [32], tuning of the resonant term is exclusively performed at the fundamental and low-order harmonic frequencies to refine the output voltage waveform quality. Nevertheless, the stabilization principles of this control technique remain unexplained. In [21], incorporation of a basic "$1/s$" integrator in series with a PR controller is proposed, expanding the stability region. This method has been successfully applied to a 400-Hz VSI system, showcasing its effectiveness for low-pulse-ratio VSIs.

This paper aims to provide a novel single-loop control scheme for autonomous VSIs, employing a PI-Lead regulator to eliminate steady-state error, improve stability, ensure fast transient response, and robustness against model parameters uncertainties, utilizing a loop shaping approach. The core contributions of this research are outlined as follows:

1) A transfer matrices-based modeling within the SRF frame is presented, enabling frequency-domain analysis via Bode plots. This approach analyses coupling terms introduced by the Park transformation in VSI model.
2) Provide a systematic design for the PI parameters to address the multi gain-crossover frequencies, ensuring a large bandwidth frequency.
3) Provide a methodical design for the Lead compensator in series with the PI regulator to address the stability-bandwidth trade-off, while considering model parameter uncertainties.
4) Ensure significant improvements in stability through the enhancement of the phase margin, infinite gain margin, maintaining large bandwidth, and ensuring controller robustness against model uncertainties.
5) Eliminate the necessity for current sensors with the most types of loads, while introducing a virtual resistor loop, to mitigate resonance and overcome the slow dynamics observed with the inductive loads.

The rest of this paper is organized as follows: Section II provides the system description, modeling, and control objectives. Section III focuses on the coupling analysis, the control design, and the robustness analysis. Section IV investigates the inductor current dynamics and the virtual resistor-based active damping. Section V presents the performance results of the proposed controller, including a comparison with the conventional PI controller. Section VI presents the experimental verification results. Finally, the conclusion is given in Section VII.

II. TOPOLOGY AND MODELING

A. SYSTEM DESCRIPTION

Fig. 1 illustrates the VSI operating in an islanded mode. This detailed schematic shows a three-phase inverter structure, comprising three separate legs. Each leg contains a combination of IGBT/Diode, forming a binary switch system: State 1 for 'ON' and State 0 for 'OFF'. Consequently, the interaction between these states in each leg creates a unique

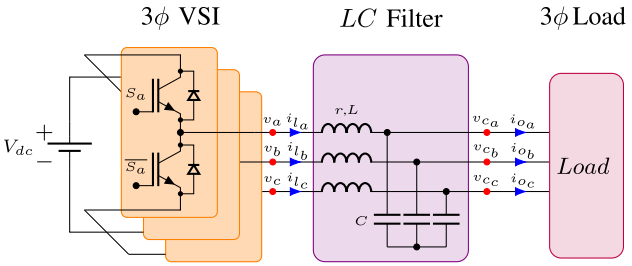

FIGURE 1. Schematic diagram of an islanded VSI.

switching pattern, making each leg an independent switch, labeled as S_j. This precise switching sequence is crucial for modulating the dc-link voltage, denoted as V_{dc}, into an AC voltage.

Furthermore, the phase voltages at the inverter bridge output exhibit a pulsed waveform. This characteristic implies the presence of higher commutation frequencies attributable to Pulse Width Modulation (PWM). Therefore, to mitigate these harmonics, a second-order low-pass LC filter can be employed. Importantly, the selection of the inductance L and capacitance C values is critical, aiming to establish a cutoff frequency significantly lower than the commutation frequency ($f_{cutoff} \ll f_{PWM}$). Adhering to this criterion is essential to ensure a sinusoidal voltage waveform at the output terminals of the LC filter's capacitors.

B. DYNAMIC MODEL

The dynamical behavior of the LC filter is comprehensively described by a set of differential equations, formulated within the SRF frame. Therefore, to enhance the understanding of the characteristics of the system's dynamics, conducting a thorough and precise input-output modeling is crucial. Furthermore, this modeling exemplifies the practical application of the SRF frame model, and enables the analysis of the system's behavior with different input frequencies, offering deeper and extensive knowledge of the system's internal dynamics.

Prior to elaborating the state-space model, the following assumptions are made

- *Assumption 1*: The switching frequency f_{PWM} is significantly higher than the natural frequencies of the power stage.
- *Assumption 2*: The inverter switches are assumed to be ideal.

The state-space model in the dq-frame, commonly used in the literature, is expressed as follows

$$\frac{\mathrm{d}}{\mathrm{d}t}\begin{pmatrix} i_l \\ v_c \end{pmatrix} = \underbrace{\begin{bmatrix} -\frac{r}{L} & \omega_0 & 0 & 0 \\ -\omega_0 & -\frac{r}{L} & 0 & 0 \\ \frac{1}{C} & 0 & 0 & \omega_0 \\ 0 & \frac{1}{C} & -\omega_0 & 0 \end{bmatrix}}_{A} \begin{pmatrix} i_l \\ v_c \end{pmatrix} + \underbrace{\begin{bmatrix} \frac{1}{L} & 0 \\ 0 & \frac{1}{L} \\ 0 & 0 \\ 0 & 0 \end{bmatrix}}_{B_1} u + \underbrace{\begin{bmatrix} 0 & 0 \\ 0 & 0 \\ -\frac{1}{C} & 0 \\ 0 & -\frac{1}{C} \end{bmatrix}}_{B_2} i_o \tag{1}$$

$$y = \underbrace{\begin{bmatrix} 0 & 0 & 1 & 0 \\ 0 & 0 & 0 & 1 \end{bmatrix}}_{C} \begin{pmatrix} i_l \\ v_c \end{pmatrix} \tag{2}$$

Here, A, B_1, B_2, and C represent the state matrix, control input matrix, disturbance input matrix, and output matrix, respectively. The state vectors are defined as $i_l = [i_{ld}, i_{lq}]^T$, representing the inductor currents, and $v_c = [v_{cd}, v_{cq}]^T$, representing the capacitor voltages. The control vector is $u = [u_d, u_q]^T$, corresponding to the output voltages of the inverter bridge, while $i_o = [i_{od}, i_{oq}]^T$ denotes the load currents. Each vector contains the direct (d) and quadrature (q) components of the respective electrical parameters. Furthermore, ω_0 is the fundamental angular frequency of the system.

The input-output relationship in the Laplace domain, obtained by applying the Laplace transformation to the state-space equations (1)–(2), is given by

$$V_c(s) = \underbrace{C(sI_4 - A)B_1}_{F(s)}\, U(s) + \underbrace{C(sI_4 - A)B_2}_{G(s)}\, I_o(s) \tag{3}$$

where I_4 denotes the 4×4 identity matrix.

Equation 3 demonstrates that the capacitor voltages v_c in the Laplace domain depend on both the control input u and the load currents i_o, as described by the system's state-space representation.

The equation (3) leads to the Laplace representation of the system, as follows

$$V_c(s) = \underbrace{\begin{bmatrix} F_1(s) & F_2(s) \\ -F_2(s) & F_1(s) \end{bmatrix}}_{F(s)} U(s) + \underbrace{\begin{bmatrix} G_1(s) & G_2(s) \\ -G_2(s) & G_1(s) \end{bmatrix}}_{G(s)} \begin{pmatrix} I_{od}(s) \\ I_{oq}(s) \end{pmatrix} \tag{4}$$

where

$$F_1(s) = \frac{LCs^2 + rCs - LC\omega_0^2 + 1}{D(s)} \tag{5}$$

$$F_2(s) = \frac{2LC\omega_0 s + rC\omega_0}{D(s)} \tag{6}$$

$$G_1(s) = -\frac{CL^2s^3 + 2rLCs^2 + (CL^2\omega_0^2 + L + Cr^2)s + r}{D(s)} \tag{7}$$

$$G_2(s) = -\frac{CL^2\omega_0 s^2 + 2rLC\omega_0 s + (CL^2\omega_0^3 - L\omega_0 + Cr^2\omega_0)}{D(s)} \tag{8}$$

With

$$D(s) = L^2C^2s^4 + 2C^2rLs^3 + (2L^2C^2\omega_0^2 + r^2C^2$$

$$+ 2LC)s^2 + (2rLC^2\omega_0^2 + 2rC)s + L^2C^2\omega_0^4 + r^2C^2\omega_0^2 - 2LC\omega_0^2 + 1 \quad (9)$$

C. CONTROL OBJECTIVES

This paper focuses on accurately controlling the capacitor voltages to be aligned with specific reference values. The goal is to maintain precise control, ensure zero steady-state error, and ensure fast controller response while maintaining sufficient stability margin. This will improve the output waveform quality, objectively measured by the Total Harmonic Distortion (THD) index. Also, the system is designed to have robustness to withstand the parameter variations and reject external disturbances, namely the load current variations, which is crucial for stable performance.

To meet the control objectives, subsequent sections will focus on the analysis of the transfer matrix that connects the capacitor voltages to the control vector. From (4), the input-output equation in the matrix form is expressed as

$$V_c(s) = F(s)\,U(s) \quad (10)$$

This approach simplifies the understanding of the control system's behavior by emphasizing the transfer function's role in achieving desired outcomes.

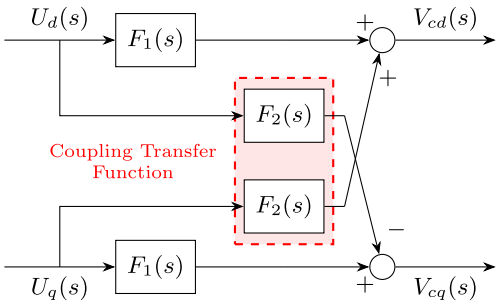

FIGURE 2. Capacitor voltages coupling characteristics.

III. PROPOSED CONTROLLER DESIGN

A. COUPLING ANALYSIS

As Fig. 2 shows, the system exhibits coupling characteristics, indicating that the variables V_{cd} and V_{cq} are both represented as functions of U_d and U_q. This relationship is mathematically formulated as follows

$$V_{cd}(s) = F_1(s)\,U_d(s) + F_2(s)\,U_q(s) \quad (11)$$
$$V_{cq}(s) = -F_2(s)\,U_d(s) + F_1(s)\,U_q(s) \quad (12)$$

To fully understand the interactions in the system, it is imperative to perform a detailed analysis of the coupling inherent in the transfer matrix $F(s)$, as this coupling may compromise the system's stability. This analysis requires comparing the diagonal and off-diagonal transfer functions to assess their relative influence. A frequency-domain evaluation using Bode plots is conducted, enabling a detailed magnitude comparison of these transfer functions. This approach offers valuable insights into the system's interactive behavior and the inter-dependencies within the matrix.

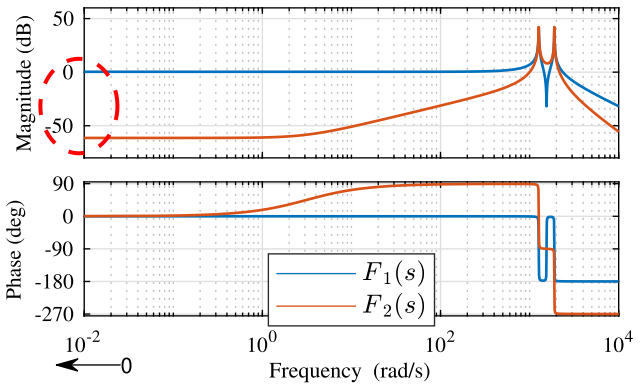

FIGURE 3. Analysis of the transfer matrix coupling of capacitor voltages.

An analysis of the magnitudes in Fig. 3 reveals that the anti-diagonal transfer functions have a very small effect on the capacitor voltages at low frequencies. However, there is a potential for amplification of the control variables' magnitude near the resonance frequencies. At high frequencies, the anti-diagonal transfer functions effectively attenuate noise and mitigate the impact of f_{PWM}.

This suggests that the system exhibits weak coupling at low frequencies, which is advantageous for our analysis since the modeling is performed in the dq-frame, where the focus is on the constant component (0 Hz). Based on this observation, the primary emphasis of this paper is on the diagonal transfer functions. Consequently, Eq. (13) plays a crucial role in the subsequent analysis

$$V_c(s) \approx F_1(s)\,U(s) \quad (13)$$

B. CONTROL DESIGN REQUIREMENTS

Prior to the controller design phase, it is crucial to analyze the stability and performance of the system. The transfer function $F_1(s)$ is characterized by four complex conjugate poles and two complex conjugate zeroes, which are defined as follows

$$z_{1,2} = -\zeta_0\omega_{n0} \pm j\omega_{n0}\sqrt{1-\zeta_0^2} \quad (14)$$
$$p_{1,2} = -\zeta_1\omega_{n1} \pm j\omega_{n1}\sqrt{1-\zeta_1^2} \quad (15)$$
$$p_{3,4} = -\zeta_2\omega_{n2} \pm j\omega_{n2}\sqrt{1-\zeta_2^2} \quad (16)$$

where

$$\zeta_0 = \frac{r}{2\sqrt{\frac{L}{C}(1-LC\omega_0^2)}} \quad (17)$$
$$\zeta_1 = \frac{r}{2\sqrt{\frac{L}{C}(1+LC\omega_0^2 - C\omega_0\sqrt{\frac{4L}{C}-r^2})}} \quad (18)$$
$$\zeta_2 = \frac{r}{2\sqrt{\frac{L}{C}(1+LC\omega_0^2 + C\omega_0\sqrt{\frac{4L}{C}-r^2})}} \quad (19)$$
$$\omega_{nj} = \frac{r}{2L\zeta_j} \quad \text{for} \quad j = 0, 1, 2 \quad (20)$$

The stable poles affirm the open-loop system stability, albeit with slow dynamics due to the small value of ζ

(i.e., $\zeta \ll 1$). Furthermore, as depicted in Fig. 4, the system demonstrates a double resonance phenomenon at frequencies $\omega_{r1} \approx \omega_{n1}$ and $\omega_{r2} \approx \omega_{n2}$, leading to three gain crossover frequencies ω_{c1}, ω_{c2}, and ω_{c3} and multiple phase margins. Despite displaying characteristics of marginal stability, as evidenced by a narrow phase margin value, the system maintains closed-loop stability.

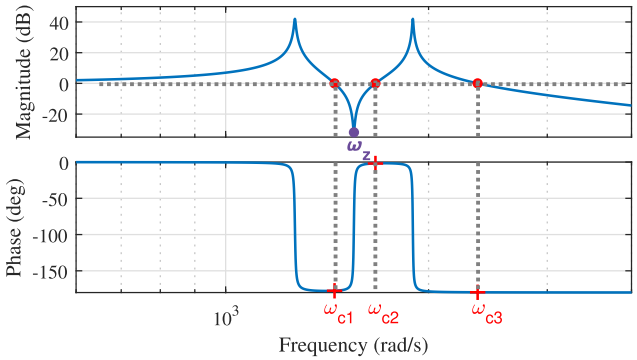

FIGURE 4. Bode plot of the studied system in open loop.

However, To achieve the outlined control objectives, it's imperative to carefully address these constraints during the controller synthesis. Specifically, to ensure zero steady-state error, the higher gain crossover frequency must coincide with the bandwidth frequency, and the phase margin (minimum $\Delta\phi$) should align with this higher gain crossover frequency.

C. PI-LEAD COMPENSATOR

1) PERFORMANCE REQUIREMENTS

In pursuit of fulfilling the objectives of eliminating steady-state error and improving system response, a PI controller has been utilized. The primary approach for determining the PI controller parameters involves loop shaping, a method centered on analyzing the open-loop transfer function $H_{ol}(s)$. Since it is assumed that the switches are ideal and the switching frequency is much higher than the natural frequencies of the system, inverter and control delays are not considered in the model [33]. Therefore, $H_{ol}(s)$ is expressed as follows

$$H_{ol}(s) = k_p(1 + \frac{1}{T_i s})\frac{LCs^2 + rCs - LC\omega_0^2 + 1}{D(s)} \tag{21}$$

The proportional gain, k_p, regulates the magnitude of the open-loop system. As illustrated in Fig. 5, increasing k_p raises the magnitude, resulting in a higher gain crossover frequency. Thus, adjusting k_p enables for precise tuning of the bandwidth frequency, or equivalently, the gain crossover frequency, $\omega_{c0} \approx 0.1\omega_{PWM}$. However, to mitigate the complexity of multiple gain crossover frequencies and ensure a unique gain crossover frequency, it is crucial to select k_p such that the magnitude at the frequency ω_z exceeds 0 dB. Therefore, the value of k_p must be constrained between k_p, min and k_p, max.

First, it has been considered that the integral term manifests only in low frequencies, so its presence does not affect the high frequencies, as shown in Fig. 6. Following this

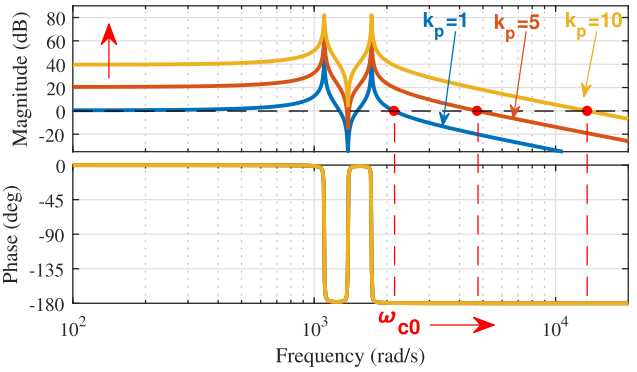

FIGURE 5. Magnitude of the open-loop system under different values of k_p.

assumption, the simplified open-loop transfer function is delineated as follows

$$H_{ol}^{s}(s) = k_p\frac{LCs^2 + rCs - LC\omega_0^2 + 1}{D(s)} \tag{22}$$

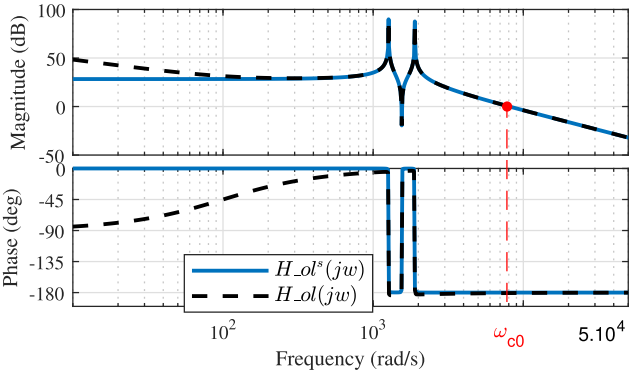

FIGURE 6. Analysis of bode plot characteristics for the open-loop transfer function $H_{ol}(j\omega)$, alongside the simplified transfer function $H_{ol}^{s}(j\omega)$.

Mathematically, the condition defining k_p can be expressed through the following equations

$$k_{p,min} < k_p \leq k_{p,max} \tag{23}$$

where

$$k_{p,min}|F(j\omega_z)| = 1 \Rightarrow k_{p,min} = \frac{1}{|F(j\omega_z)|} \tag{24}$$

And

$$k_{p,max}|F(j\omega_{c0})| = 1 \Rightarrow k_{p,max} = \frac{1}{|F(j\omega_{c0})|} \tag{25}$$

Substituting (24) and (25) into (23) yields

$$\frac{1}{|F(j\omega_z)|} < k_p \leq \frac{1}{|F(j\omega_{c0})|} \tag{26}$$

This condition holds true only if $|F(j\omega_{c0})| < |F(j\omega_z)|$.

The integral term, T_i, plays a key role in achieving zero steady-state error by providing infinite gain at low frequencies. Selecting a sufficiently large value for T_i is recommended to expedite the reduction of steady-state error [34]. However, as T_i introduces a $-90°$ phase shift

that diminishes with increasing frequency, its value must be carefully chosen to avoid interference with resonant frequencies and to preserve phase margin, ensuring system stability. A practical choice is to set T_i to ten times larger than the time constant of the first resonance, T_{r1}, as expressed in the following equation

$$10.\omega_i = \omega_{r1} \tag{27}$$

Thus, the value of T_i is determined as follows

$$T_i = \frac{2\pi.10}{\omega_{r1}} \tag{28}$$

2) STABILITY REQUIREMENTS

The stability of the system can be effectively achieved through the incorporation of a lead compensator into the open-loop system. It allows an augmentation in the phase margin, denoted as $\Delta\phi$, particularly in the vicinity of the cut-off frequency ω_{c0}. Consequently, this adjustment is reflected in (21), which is presented as follows

$$H_{ol}(s) = k_p(\frac{1+\alpha\tau s}{1+\tau s})(1+\frac{1}{T_i s})\frac{LCs^2+rCs-LC\omega^2+1}{D(s)} \tag{29}$$

where $\alpha > 1$ and τ are the parameters of the lead compensator that can be calculated through the expressions

$$\alpha = \frac{1+sin(\phi_{max})}{1-sin(\phi_{max})} \tag{30}$$

$$\tau = \frac{1}{\omega_{max}\sqrt{\alpha}} \tag{31}$$

As delineated in (30)-(31), ϕ_{max} signifies the maximum phase shift needed to attain the designated phase margin, as expressed by

$$\phi_{max} = \Delta\phi - \phi(\omega_{c0}) - \pi \tag{32}$$

The parameter $\omega_{\max}$ signifies the frequency at which the maximum phase shift $\phi_{\max}$ manifests. Notably, this frequency is carefully placed to coincide with the cutoff frequency ω_{c0}, as illustrated in Fig.7.

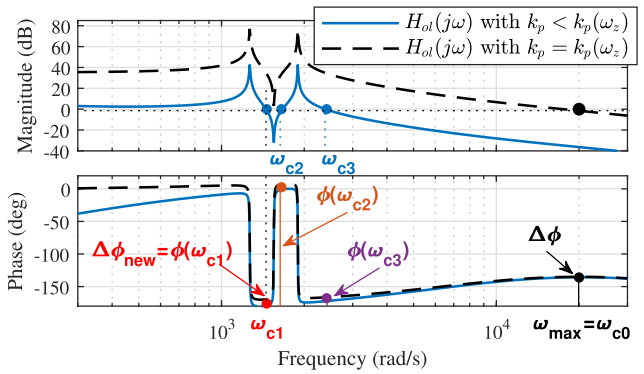

FIGURE 7. Bode plot based analysis of the system with the PI-Lead compensator in case of different k_p values.

3) ROBUSTNESS REQUIREMENTS

The stability of the system may be compromised due to either improper tuning of the PI compensator gain, k_p, or internal disturbances arising from parameter mismatch of the LC filter components (i.e., $C = C_n + \Delta C$ and $L = L_n + \Delta L$, with ΔC and ΔL representing parametric uncertainties, while C_n and L_n denoting nominal values). This compromise is observable as a downward shift in the magnitude curve, as illustrated in Fig. 8. Such a shift leads to the emergence of multiple gain crossover frequencies, thereby causing a deviation of the phase margin, $\Delta\phi_{new}$, from the desired value set by the lead compensator. The $\Delta\phi_{new}$, adopt the minimum phase among those corresponding to the gain crossover frequencies, expressed as

$$\Delta\phi_{new} = min(\phi(\omega_{c1}), \phi(\omega_{c2}), \phi(\omega_{c3})) \approx \phi(\omega_{c1}) \tag{33}$$

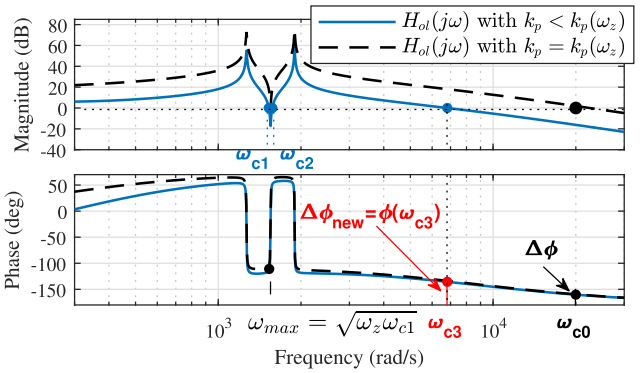

FIGURE 8. Bode plot based analysis of the system with the PI-Lead compensator, highlighting the stability and the bandwidth enhancement.

To enhance the system's robustness against internal disturbances, maintain stability margins, and alleviate cutoff frequency displacement, it is imperative to minimize the phase at the highest gain crossover frequency, as depicted in Fig. 8. Practically, this can be accomplished by choosing ω_{max} in close proximity to ω_z to ensure that $\phi(\omega_{c3}) < min(\phi(\omega_{c1}), \phi(\omega_{c2}))$. Expressing ω_{max} can be outlined as follows

$$\omega_{max} = \sqrt{\omega_z\omega_{c1}} \tag{34}$$

4) SYSTEM PERFORMANCE ASSESSMENT

The system's performance in reference tracking and disturbance rejection can be evaluated through the frequency response of the capacitor voltage error $E(s)$, defined as the difference between the reference input $V_c^*(s)$ and the actual output $V_c(s)$. The relationship among $E(s)$, $V_c^*(s)$, and the output current disturbance $I_o(s)$ is given by:

$$E(s) = \underbrace{\frac{1}{1+F_1(s)C(s)}}_{E_1(s)} V_c^*(s) + \underbrace{\frac{-G_1(s)}{1+F_1(s)C(s)}}_{E_2(s)} I_o(s) \tag{35}$$

Here, $C(s)$ represents the PI-Lead controller transfer function, while $E_1(s)$ and $E_2(s)$ are the sensitivity transfer

functions for the capacitor voltage reference input and the output current disturbance, respectively.

Fig. 9 and Fig. 10 depict the frequency response of $E(s)$ for the reference input $V_c^*(s)$ and the output current disturbance $I_o(s)$, respectively. The Bode plot of $E_1(s)$ (Fig. 9) demonstrates that the steady-state error converges to $-\infty$ dB at $\omega = 0$ rad/s, corresponding to $E_s = 0$, confirming the system's effectiveness in tracking the reference. Similarly, the Bode plot of $E_2(s)$ (Fig. 10) shows a steady-state error tending to $-\infty$ dB at $\omega = 0$ rad/s, indicating robust rejection of output current disturbances.

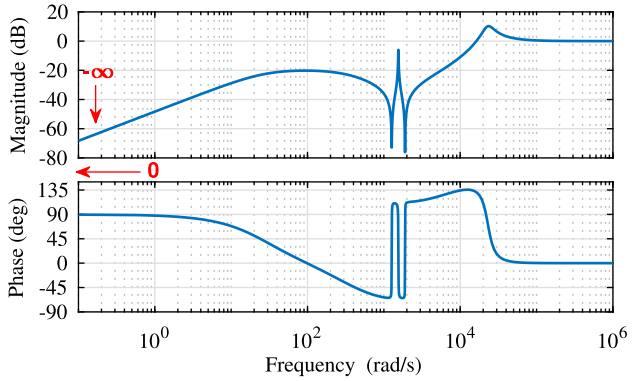

FIGURE 9. Frequency response of the capacitor voltage error $E(s)$ with respect to the reference $V_c^*(s)$.

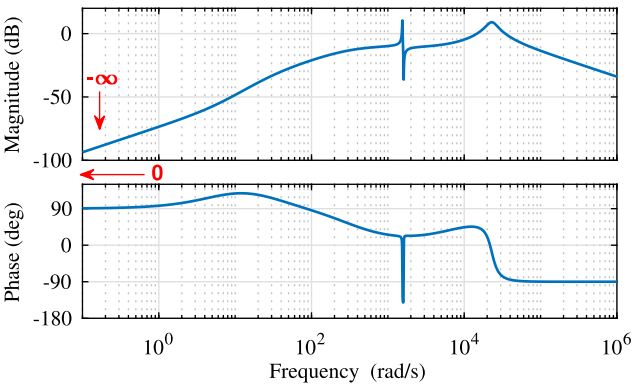

FIGURE 10. Frequency response of the capacitor voltage error $E(s)$ with respect to the disturbance $I_o(s)$.

IV. INDUCTOR CURRENTS DAMPING

A. INDUCTOR CURRENTS DYNAMICS

The proposed PI-Lead compensator has been incorporated into the control loop, with the specific objective of achieving precise control over the capacitor voltages within a single-loop configuration. In contrast to the conventional cascaded control loop, the inductor current dynamics are treated as internal and omitted during the design process. Given that the capacitor voltage dynamics respond relatively slowly to control actions, the natural current dynamics remain largely unaffected by the loop. Their behavior can thus be assessed a posteriori by examining their natural dynamics while assuming constant capacitor voltages, substantiated by singular perturbation theory [35]. The governing equations for the current dynamics are as follows

$$\frac{d}{dt}\begin{pmatrix} i_{ld} \\ i_{lq} \end{pmatrix} = \begin{bmatrix} -\frac{r}{L} & \omega_0 \\ -\omega_0 & -\frac{r}{L} \end{bmatrix} \begin{pmatrix} i_{ld} \\ i_{lq} \end{pmatrix} + \frac{1}{L}\begin{pmatrix} v_d \\ v_q \end{pmatrix} - \frac{1}{L}\begin{pmatrix} v_{cd} \\ v_{cq} \end{pmatrix} \tag{36}$$

The dynamic behavior of the inductor currents exhibits asymptotic stability, a conclusion drawn from the analysis of the characteristic equation $P(\lambda) = \lambda^2 + \frac{2r}{L}\lambda + \frac{r^2}{L^2} + \omega_0^2$, which is Hurwitz-stable. However, this equation reveals the existence of undesirable oscillations during the transient state, a phenomenon which is attributed to the very small damping ratio $\zeta \approx \frac{r}{L\omega_0}$.

To mitigate this issue, an inductor current state-feedback is incorporated into (36). This realization aims to enhance the internal stability of the system.

$$v_{dq} = -Ki_{ldq} + u_{dq} \tag{37}$$

where K is the inductor current state feedback gain, and u_{dq} is given by its input-output equation

$$U_{dq}(s) = \left(\frac{1+\alpha\tau s}{1+\tau s}\right)\left(k_p + \frac{1}{T_i s}\right)\left(V_{cdq}^*(s) - V_{cdq}(s)\right) \tag{38}$$

(37) modifies the control law by incorporating state feedback. It is essential to verify that the system characteristics remain unchanged. Fig. 11 clearly illustrates that the addition of the inductor current feedback mainly affects the resonance magnitude, leading to an enhancement of the transient response performance.

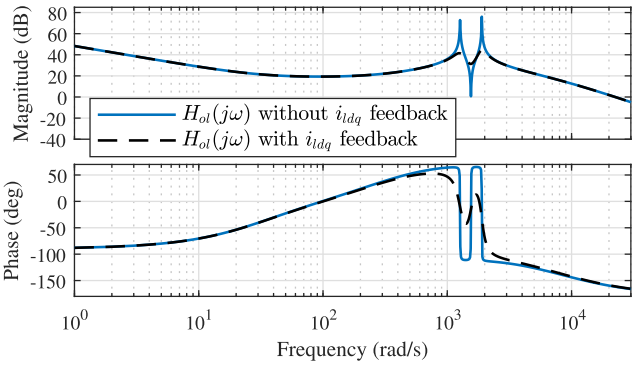

FIGURE 11. The bode plot of the open-loop system with and without i_{ldq} feedback.

B. VIRTUAL RESISTOR BASED ACTIVE DAMPING

To delve deeper into the examination of the transient phase within the dynamics of inductor currents', the focus is directed towards the analysis of an inverter represented by a voltage source interlinked with an *rLrC* filter, featuring an inductive load as illustrated in Fig. 12.

The transfer function of the inductor currents in the dq frame is given by

$$\frac{I_{ldq}(s)}{V_{eqd}(s)} = \frac{a_4 s^4 + a_3 s^3 + a_2 s^2 + a_1 s + a_0}{b_6 s^6 + b_5 s^5 + b_4 s^4 + b_3 s^3 + b_2 s^2 + b_1 s + b_0} \tag{39}$$

where

$$\begin{aligned}
a_4 &= C^2 L L_l^2 \omega_0 \\
a_3 &= 2C^2 L L_l R_c \omega_0 + 2C^2 L L_l R_l \omega_0 \\
a_2 &= L\omega_0 C^2 R_c^2 + 2L\omega_0 C^2 R_c R_l + L\omega_0 C^2 R_l^2 + 2LL_l\omega_0 C \\
a_1 &= 2CLR_c\omega_0 + 2CLR_l\omega_0 + CL_l R_c\omega_0 - 2C^2 L L_l R_c \omega_0^3 \\
&\quad - 2C^2 L L_l R_l \omega_0^3 \\
a_0 &= -LC^2 L_l^2 \omega_0^5 - LC^2 R_c^2 \omega_0^3 - 2LC^2 R_c R_l \omega_0^3 - LC^2 R_l^2 \omega_0^3 \\
&\quad + CL_l R_c \omega_0^2 + L_l\omega_0 + L\omega_0 \\
b_6 &= C^2 L^2 L_l^2 \\
b_5 &= 2C^2 L L_l^2 R + 2C^2 L^2 L_l R_c + 2C^2 L^2 L_l R_l \\
b_4 &= C^2 L^2 L_l^2 \omega_0^2 + C^2 L^2 (R_c^2 + R_l^2) + 4C^2 L L_l R (R_c + R_l) \\
&\quad + 2C^2 L^2 R_c R_l + C^2 L_l^2 R^2 + 2C(L_l L^2 + L L_l^2) \\
b_3 &= 2C^2 LR(R_c^2 + R_l^2) + 2CL_l(LR_c + L_l R) + 2CL^2(R_c + R_l) \\
&\quad + 2C^2 L_l R^2 (R_l + R_c) + 4C^2 LRR_c R_l + 4CLL_l(R_l + R) \\
b_2 &= -C^2 L^2 L_l^2 \omega_0^4 - 4C^2 L L_l R \omega_0^2 (R_c + R_l) + C^2 R^2 (R_c^2 + R_l^2) \\
&\quad + 2C^2 R^2 R_c R_l + 2C\omega_0^2 (L^2 L_l + L_l^2 L) + 4CLR(R_c + R_l) \\
&\quad + 2CLR_l(R_c + R_l) + 2CL_l R(R_c + R) + 4CL_l R R_l + 2LL_l \\
&\quad + L^2 + L_l^2 \\
b_1 &= -2C^2 L L_l \omega_0^4 (LR_c + LR_l + L_l R) - 2C^2 LR\omega_0^2 (R_c^2 + R_l^2) \\
&\quad - 2C^2 L_l R^2 \omega_0^2 (R_c + R_l) - 4C^2 LRR_c R_l \omega_0^2 + 2CR^2 (R_c + R_l) \\
&\quad + 2CL^2 \omega_0^2 (R_c + R_l) + 2CL_l \omega_0^2 (LR_c + L_l R) + 2L(R + R_l) \\
&\quad + 2CRR_l(R_l + R_c) + 2L_l(R + R_l) \\
b_0 &= -C^2 L^2 L_l^2 \omega_0^6 - C^2 L^2 \omega_0^4 (R_c^2 + 2R_c R_l + R_l^2) \\
&\quad - C^2 L_l^2 R^2 \omega_0^4 - C^2 R^2 \omega_0^2 (R_c^2 + 2R_c R_l + R_l^2) \\
&\quad + \omega_0^2 (L^2 + 2LL_l + L_l^2) + R^2 + 2RR_l + R_l^2
\end{aligned}$$

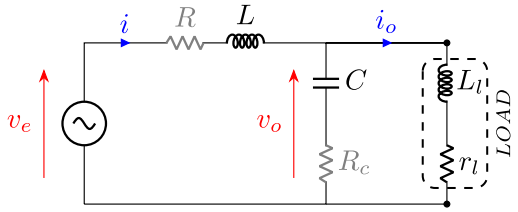

FIGURE 12. Schematic diagram of an *rLrC*-filtered inverter with inductive load.

Fig. 13 illustrates the Bode plot of the inductor current's transfer function as described in (39). The plot reveals three resonance peaks at ω_{res_1}, ω_{res_2} and ω_{res_3}, occurring at high frequencies. These resonance peaks indicate that the transient dynamics of the currents may exhibit overshoot and a slower response.

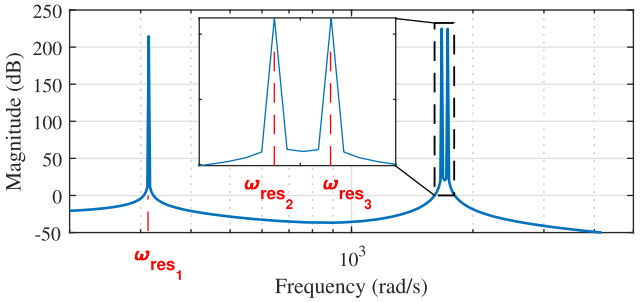

FIGURE 13. Bode plot of the inductor currents' transfer function.

The examination of the considered system involves a comprehensive analysis achieved by varying the parameters inherent to its structure. These parameters encompass the resistances denoted as R, R_c, as well as the inductance denoted as L, and the capacitance denoted as C.

In Fig. 14(a)-14(b), an examination of system parameters L and C variations is undertaken, specifically with resistances set to zero. The resonance frequency is intricately linked to these parameters. Such a phenomenon is likely to influence the dynamics of both inductive and load currents significantly, especially the transient phase.

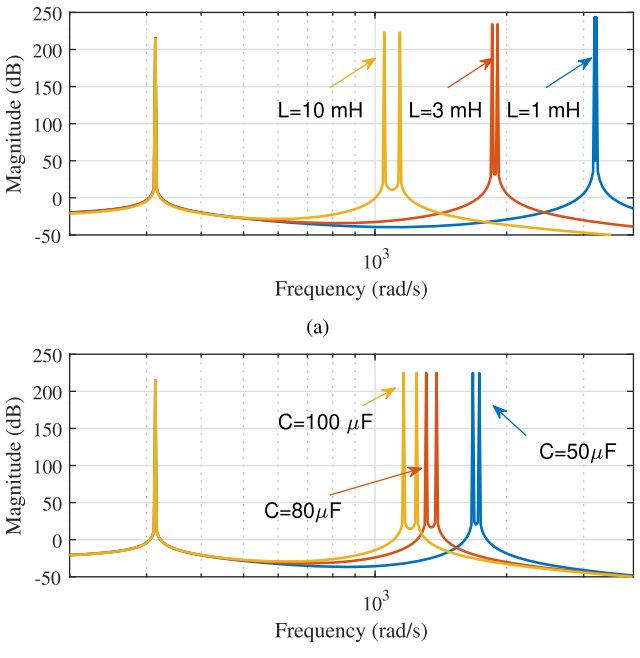

FIGURE 14. Analysis of parameter variations in the *rLrC* Filter impact with consistent values of other components. Variation of (a) the inductance L (b) the capacitance C.

To mitigate the resonance phenomenon, a variation in the resistance values was implemented. Figure 15(a) illustrates the relationship between the increased resistance value of the resistor connected in series with the capacitor, R_c. The impact of this increase is particularly evident at ω_{res_2} and ω_{res_3}, while the resonance at ω_{res_1} remains unaffected. This indicates that increasing the value of R_c does not improve the transient dynamics because the first resonance peak

is primarily generated by the dominant complex conjugate poles. This conclusion is further supported by Figure 16(a), which shows that increasing R_c from 0 to 0.5 enhances the stability of the poles responsible for resonances 2 and 3. However, the poles associated with resonance 1 remain unaffected by this increase in R_c value. Therefore, it is crucial to avoid introducing a resistor in series with the *LC* filter capacitor.

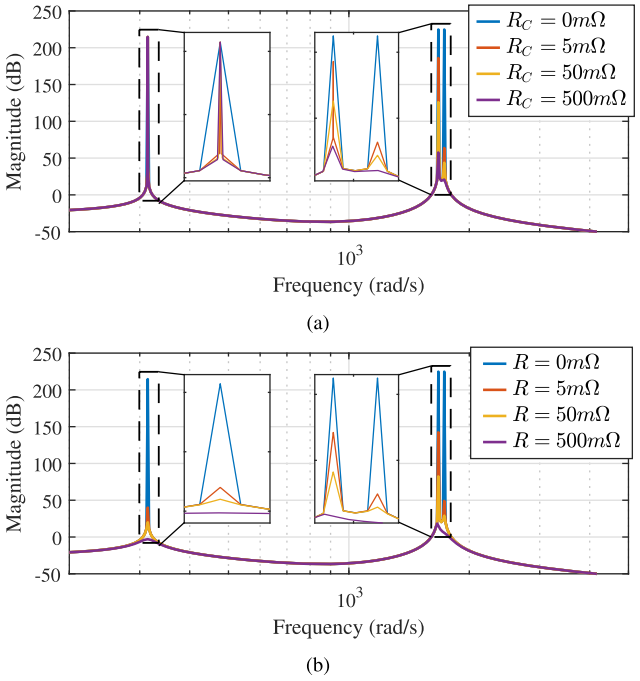

FIGURE 15. Analysis of Parameter Variations in the *rLrC* Filter impact with consistent values of other components. Variation of (a) the capacitor resistance R_c (b) the inductor resistance R.

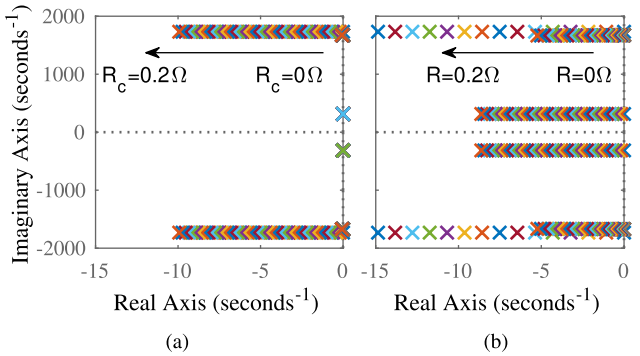

FIGURE 16. Open-loop stability investigation in case of (a) increasing the value of the resistance R_c (b) increasing the value of the resistance R.

Figure 15(b) illustrates the impact of increasing the resistance value R in the *LC* filter on attenuating resonance phenomena. The increase in resistance value reduces the magnitude at all resonance frequencies. Moreover, Fig. 16(b) demonstrates that the enhancement in the resistance not only contributes to the suppression of resonance but also plays a pivotal role in augmenting the stability of the open-loop system. This adjustment simultaneously leads to an improvement in the dynamic response time of the system, thereby indicating a direct correlation between the resistance increment and system performance enhancement.

Incorporating this solution into the controller to improve the dynamics of inductor currents is highly beneficial. However, the addition of a physical resistor in series with the inductor within an *LC* filter leads to undesirable power losses. Consequently, the use of a virtual resistor emerges as a strategic alternative, utilizing its influence on enhancing current dynamics without incurring power dissipation. The deployment of a virtual resistor is effectively a practical application of the previously proposed inductor current state feedback. This approach is supported through the implementation of the virtual resistor in the controller, which serves as a concrete representation of state feedback. Within this context, the coefficient K in (37) can be adjusted to the necessary resistance value, thereby optimizing the dynamics of the inductor current.

V. SIMULATION RESULTS

To evaluate the performance of the proposed controller, simulations were conducted using MATLAB/Simulink software. The power stage parameters are detailed in Table 1. The performance of the proposed PI-Lead controller was compared with that of a conventional PI-PI dual-loop controller. For the PI-Lead controller, the parameters were set as $k_p = 15$, $k_i = 150$, $\alpha = 20$, and $\tau = 2.10^{-5}$. For the PI-PI dual-loop controller, the current loop parameters were $k_{pi} = 0.18$ and $k_{ii} = 1.7.10^3$, while the voltage loop parameters were $k_{pv} = 0.04$ and $k_{iv} = 19.74$. The evaluation included three test scenarios: the controllers' response to a linear load, performance under voltage reference variations, and robustness against parameter mismatches for both linear and nonlinear loads.

TABLE 1. Parameters of the islanded three-phase inverter system.

Switching frequency	f_{sw}	$20\,kHz$
Sampling frequency	$f_s = 2f_{sw}$	$40\,kHz$
Fundamental frequency	f_0	$50Hz$
Dc-link voltage	V_{dc}	$250\,V$
LC-filter inductance	L	$1.58\,mH$
LC-filter series resistance	r	$0.5\,\Omega$
LC-filter capacitance	C	$50\,\mu F$

A. RESPONSE TO LINEAR LOAD

Fig. 17 illustrates the voltage waveforms across the capacitors in the SRF frame, highlighting the response of the PI-Lead and PI-PI controllers to a linear load with a resistance of $R = 38\,\Omega$ and an inductance of $L = 50\,\text{mH}$. The results clearly show that the capacitor voltages closely follow the reference signal. The PI-Lead controller demonstrates a faster response time compared to the PI-PI controller. This improvement is attributed to the single-loop structure of the PI-Lead

controller, which provides a higher bandwidth compared to the dual-loop structure of the PI-PI controller, where the voltage loop bandwidth is constrained to be lower than that of the current loop. Furthermore, Fig. 18 demonstrates the superior performance of the PI-Lead controller over the PI-PI controller in terms of harmonic distortion, with the PI-Lead controller achieving a significantly lower THD of 0.74% compared to 1.26% for the PI-PI controller.

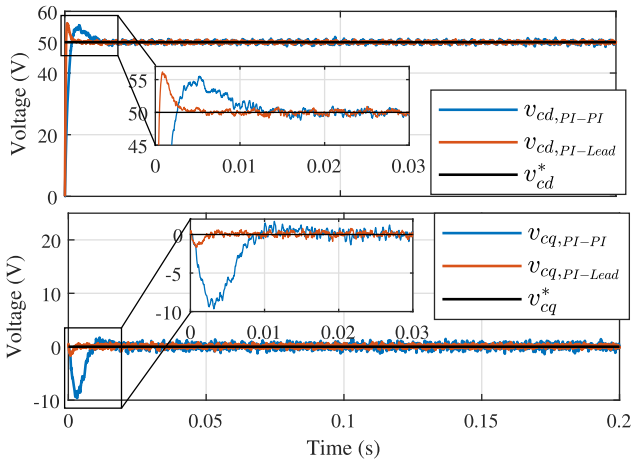

FIGURE 17. Simulation results of the capacitor voltage waveforms in the SRF frame for the PI-Lead controller and the PI-PI controller.

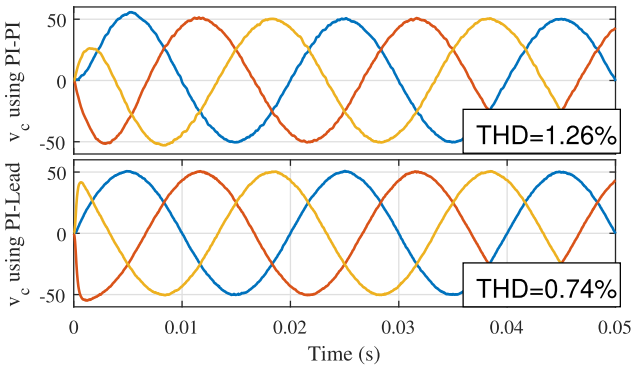

FIGURE 18. Simulation results of the capacitor voltage waveforms in the *abc* frame for the PI-Lead controller and the PI-PI controller.

B. RESPONSE TO REFERENCE VOLTAGE VARIATION

Fig. 19 presents the voltage waveforms across the capacitors in the SRF frame, illustrating a scenario where the capacitor voltage reference, v_c^*, transitions from 50 V to 85 V under the same linear load. The results clearly show that the capacitor voltages closely follow the reference signal, with the PI-Lead controller demonstrating a notably faster response time compared to the PI-PI controller. Similarly, Fig. 20 displays the voltage waveforms in the *abc* stationary reference frame for a voltage transition from 50 V to 85 V. The transition appears smooth for both controllers. However, in terms of performance quality, the PI-Lead controller outperforms the PI-PI controller, achieving a THD of 1.03% compared to 1.74% for the PI-PI controller.

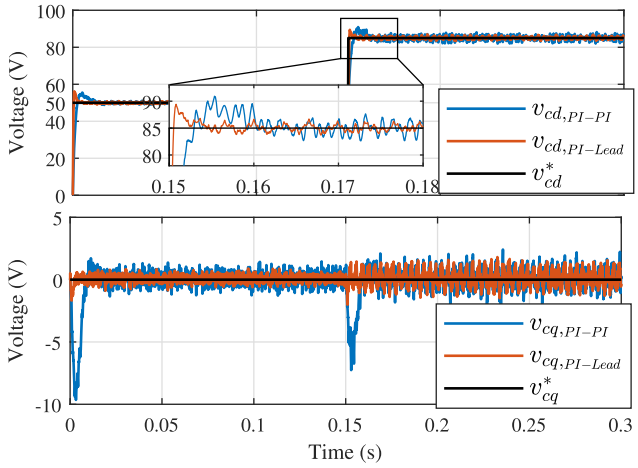

FIGURE 19. Simulation results of the capacitor voltage waveforms in the SRF frame, showing the response to reference variation for both the PI-Lead and PI-PI controllers.

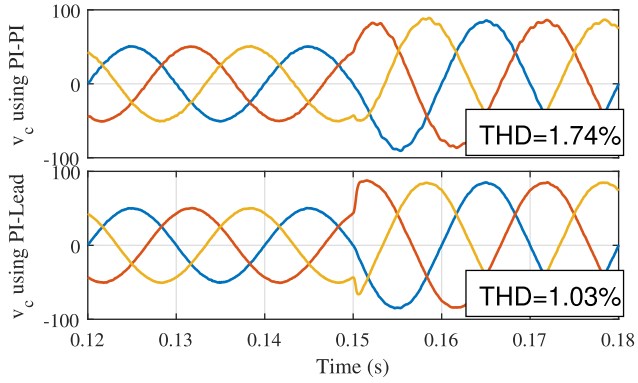

FIGURE 20. Simulation results of the capacitor voltage waveforms in the *abc* frame, showing the response to reference variation for both the PI-Lead and PI-PI controllers.

C. ROBUSTNESS AGAINST MODEL PARAMETER UNCERTAINTIES

To evaluate the effectiveness of the proposed PI-Lead controller in handling model parameter uncertainties, variations in the inductance (L) and capacitance (C) parameters were introduced within a range of 0% to 40% relative to the nominal values (L_n and C_n) of the LC filter. Table 2 presents the THD values of the capacitor voltages under these parameter variations for two load scenarios: linear and nonlinear. The results demonstrate that the PI-Lead controller exhibits strong robustness against model parameter uncertainties across both load types. In contrast, the PI-PI controller shows reduced robustness, particularly under nonlinear load conditions, where its performance significantly deteriorates compared to the PI-Lead controller.

D. COMPARATIVE ANALYSIS

Table 3 provides a detailed comparison of the proposed control strategy against two established methods from the literature, specifically for controlling an islanded inverter. This evaluation aims to highlight the three primary contributions of this paper: enhanced bandwidth, improved stability

TABLE 2. THD values (in %) from simulations with respect to model parameter uncertainties.

Parameter variation	Controller	Linear load	Nonlinear load
$L = L_n, C = C_n$	PI-Lead	0.74	0.74
	PI-PI	1.26	4.05
$L = 90\% L_n$	PI-Lead	0.83	0.83
	PI-PI	1.48	4.02
$L = 80\% L_n$	PI-Lead	1.02	1.12
	PI-PI	1.58	4.04
$L = 70\% L_n$	PI-Lead	1.23	1.25
	PI-PI	1.87	4.28
$L = 60\% L_n$	PI-Lead	1.56	1.56
	PI-PI	2.02	4.28
$C = 90\% C_n$	PI-Lead	0.85	0.82
	PI-PI	1.36	4.43
$C = 80\% C_n$	PI-Lead	1.08	0.97
	PI-PI	1.64	5.07
$C = 70\% C_n$	PI-Lead	1.32	1.18
	PI-PI	1.74	5.49
$C = 60\% C_n$	PI-Lead	1.42	1.52
	PI-PI	2.03	6.2

margins, and increased robustness. The reference methods include a hybrid reference frame-based controller employing a PI controller in the outer loop and a gain in the inner loop (HRF-PI) [36], and an optimized design-based controller utilizing a PR controller for the outer loop and a gain for the inner loop (O-PR) [22]. While these strategies employ dual-loop control, the proposed strategy employs a single-loop control, allowing it to achieve a larger bandwidth frequency of $1.2\,10^4$ rad/s, compared to lower values for the other strategies. The proposed control strategy exhibits a significant phase margin of $\Delta\phi = 41^o$, attributed to the use of a lead compensator. Additionally, the proposed method demonstrates an infinite gain margin ΔG in contrast to the small values observed in the other strategies. Three scenarios were considered with a 100Ω resistive load, addressing parameter uncertainties of C_f and L_f at 0%, +40%, and −40%, respectively. In all three scenarios, the proposed controller achieves lower voltage THD compared to the other strategies, confirming the superior performance quality and robustness of the proposed controller.

Table 4 summarizes the main advantages and disadvantages of various strategies. The proposed controller offers significant advantages over existing methods, particularly in terms of stability, as it ensures an infinite gain margin and a sufficient phase margin. Additionally, the proposed controller excels in response speed, evidenced by its larger bandwidth frequency. This is due to the lack of constraints on the single-loop bandwidth, except for those imposed by the switching frequency. Moreover, the proposed control strategy eliminates the need for current sensors in most load scenarios, except for inductive loads where active damping is required.

VI. EXPERIMENTAL RESULTS AND DISCUSSION

This section presents a detailed analysis of the obtained results to assess the effectiveness of the proposed control strategy depicted in Fig. 21(a). The experimental test bench

TABLE 3. Performance comparison of various control techniques.

Control strategy	HRF-PI [36]	O-PR [22]	Proposed method
Loop Multiplicity	double	double	Single
Voltage loop Bandwidth (rad/s)	$1.8\,10^3$	968	$1.2\,10^4$
$\Delta\phi$	46^o	35^o	41^o
ΔG	8.3 dB	4.8 dB	∞
THD (0% of C_n, L_n)	2.73 %	1.95 %	1.89 %
THD (+40% of C_n, L_n)	2.81 %	2.18 %	1.71 %
THD (-40% of C_n, L_n)	4.72 %	3.16 %	2.33 %

(Fig. 21(b)) consists of a control stage incorporating a dSpace 1104 platform and Matlab/Simulink software, while the power stage consists of the electrical components, including a SEMITEACH 08753450BE three-phase inverter from SEMIKRON and a three-phase LC filter. The control algorithm is executed through Simulink software on the dSpace 1104 platform, converting digital command signals into analog signals within a range of 0V to 5V. These signals are then amplified to 0V to 15V before being transmitted to the inverter. This amplification is performed by an amplification board, utilizing an HCPL-2200 optocoupler to ensure optical isolation between the control and power stages. The parameters selected for the experimental test bench are detailed in Table 1.

A. REFERENCE VOLTAGE VARIATION

Fig. 22(a) depicts voltage waveforms across capacitors in the SRF frame, representing a scenario where the capacitor voltage reference V_c^* shifts from $40V$ to $60V$ under a resistive load with a resistance of 38Ω. It is evident that the capacitor voltages track the reference signal, exhibiting a small transient overshoot. In Fig. 22(b), the same scenario results are presented in the *abc* stationary reference frame, where the voltage transition from $40V$ to $60V$ appears smooth, characterized by a fast transient response and a low THD value of 1.82%.

B. LOAD VARIATION

To assess the proposed controller in response to varied load conditions, two distinct scenarios were methodically examined. Initially, Fig. 23 presents the capacitor voltages in an unloaded scenario, succeeded by the introduction of a resistive load with a resistance of 38Ω. The transition exhibited smoothness, characterized by a fast transient response and a low THD value of 1.82%. Subsequently, the second scenario involved load variation, transitioning from a resistive load with a resistance of 38Ω to one with 80Ω. Fig. 24 depicts the capacitor voltages waveform, revealing consistent voltage performance, with a sustained THD value of 1.82%. This observation underscores the robustness of the proposed controller against fluctuations in load conditions.

TABLE 4. Comparison of Advantages/Disadvantages of various techniques with the proposed control strategy.

Control scheme	Features/Advantages	Drawbacks/Disadvantages
Hybrid reference frame-based dual loop control [36]	• Robustness against control delays. • Robustness against model uncertainties.	• Limited gain margin. • Limited bandwidth frequency. • High THD values.
Optimized Parameter for the dual loop control [22]	• Optimized parameter configuration for improved performance. • Minimal controller parameters tuning.	• Narrow gain margin. • Limited bandwidth frequency. • Lack of performance and robustness analysis.
Proposed PI-Lead single loop control strategy	• Robustness against model uncertainties. • Large bandwidth frequency. • Infinite gain margin. • Low THD values.	• Requires active damping in case of inductive loads.

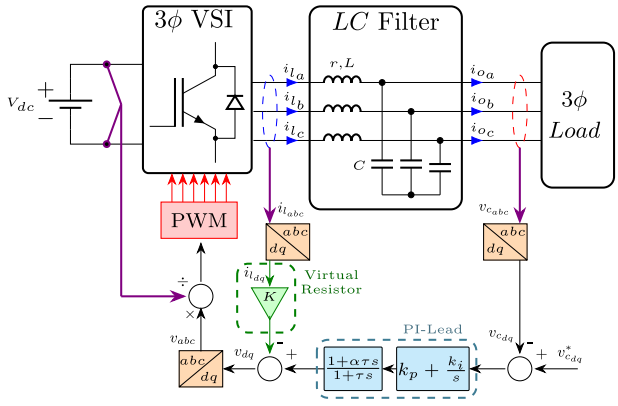

(a)

(b)

FIGURE 21. (a) Schematic diagram of a three-phase VSI with PI-Lead voltage controller with a virtual resistor. (b) Experimental setup of the islanded three-phase inverter system.

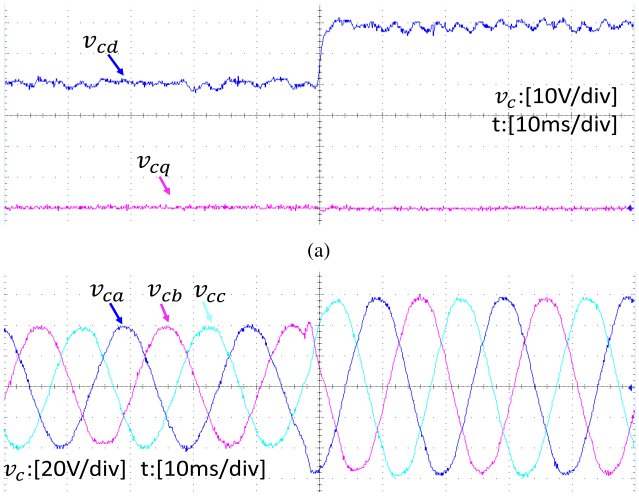

(a)

(b)

FIGURE 22. Experimental results of the capacitor voltage waveforms in: (a) the SRF frame. (b) the *abc* stationary reference frame.

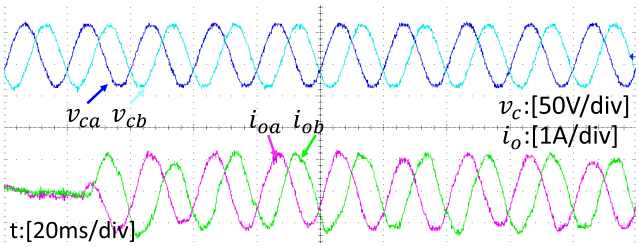

FIGURE 23. Experimental results of output voltage dynamics in response to resistive load.

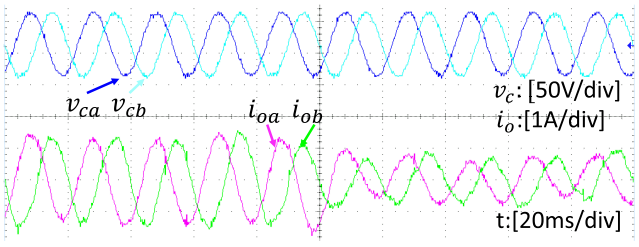

FIGURE 24. Experimental results of output voltage dynamics in response to varied load fluctuations.

C. UNBALANCED LOAD

Fig. 25 depicts the voltage waveform across capacitors in the scenario of an unbalanced load. The observed waveforms serve as evidence of the controller's efficiency in rejecting disturbances arising from the failure of a phase in the output current of a resistive load, thereby ensuring unaffected voltage performance with a low THD value of 1.93%.

D. NONLINEAR LOAD

Fig. 26 showcases the capacitor voltage performance in response to a nonlinear load. The experiment employed a nonlinear load comprising a 6-diode bridge integrated within the SEMITEACH 08753450BE inverter, coupled with a resistor of $R_l = 240\Omega$. The waveform exhibits a fast transient response, with the THD experiencing a slight rise, peaking at 1.86%, which remains significant. This conducted test proves the capability of the proposed controller to reject nonlinear disturbances.

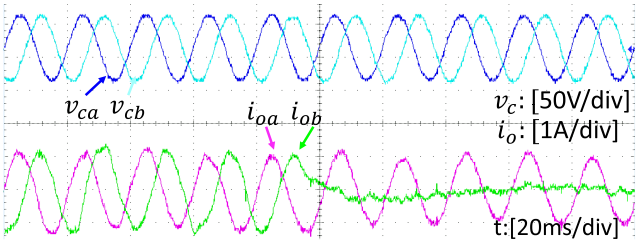

FIGURE 25. Experimental results of the dynamic response of the output voltage to unbalanced load.

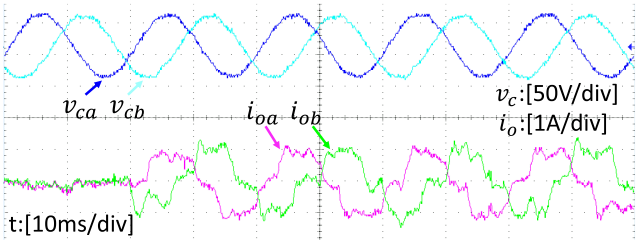

FIGURE 26. Experimental results of the dynamic response of the output voltage to nonlinear load.

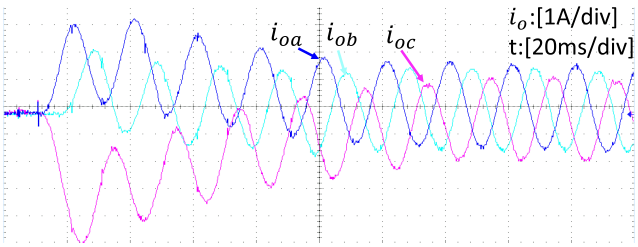

FIGURE 27. Experimental results of the output current in case of inductive load without virtual resistor.

E. INDUCTIVE LOAD

The illustration of output current dynamics in the case of inductive load characterized by parameters $L_l = 177mH$ and $R_l = 6\Omega$, without the use of the virtual resistor, is presented in Fig. 27. The observed dynamics showcase a slow response with transient overshoot, thus confirming the analysis outlined in Section IV. Fig. 28 illustrates the output current dynamics when incorporating a virtual resistor with the PI-Lead controller scheme, using a gain of $K = 150$. The resulting waveform exhibits a rapid and smooth transient response, thereby substantiating the effectiveness of employing a virtual resistor to enhance transient response characteristics.

F. ROBUSTNESS AGAINST MODEL PARAMETER UNCERTAINTIES

To assess the efficacy of the proposed PI-Lead controller in mitigating model parameter uncertainties, variations in the inductance L and capacitance C parameters in the controller part were introduced within a range of 0% to 40% relative to the nominal values L_n and C_n of the LC filter. Table. 5, shows the capacitor voltages THD

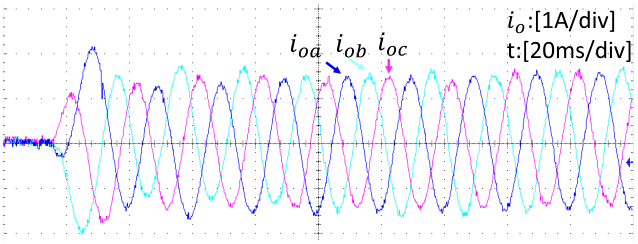

FIGURE 28. Experimental results of the output current in case of inductive load with virtual resistor, $K = 150$.

TABLE 5. THD values (in %) with respect to model parameter uncertainties.

Parameter variation	Resistive load	Unbalanced load	Nonlinear load
$L = L_n, C = C_n$	1.82	1.93	1.86
$L = 90\% L_n$	1.95	1.97	1.95
$L = 80\% L_n$	2.05	2.08	2.05
$L = 70\% L_n$	2.30	2.23	2.19
$L = 60\% L_n$	2.43	2.45	2.38
$C = 90\% C_n$	1.95	2.04	1.88
$C = 80\% C_n$	1.99	2.09	2.05
$C = 70\% C_n$	2.16	2.20	2.23
$C = 60\% C_n$	2.36	2.43	2.31

values under each model parameter variation with three load scenarios: resistive, unbalanced, and nonlinear. The results prove the robustness of the proposed controller against model parameter uncertainties for the different types of loads, particularly demonstrating notable performance under unbalanced and nonlinear load conditions.

VII. CONCLUSION

This paper proposed a novel single-loop PI-Lead control strategy to enhance voltage stability and improve current dynamics in islanded inverters, addressing key limitations found in existing approaches, such as narrow gain margins, trade-offs between stability and bandwidth, and restricted bandwidth capabilities. The proposed controller, formulated within the SRF frame, effectively manages coupling terms and multiple gain crossover frequencies through a systematic design using Bode plot-based frequency analysis. This approach yielded significant improvements in stability margins, bandwidth frequency, reduced THD, and robustness against variations in model parameters. Additionally, the control strategy eliminated the need for current sensors, except for inductive loads where a virtual resistor is employed for active damping. Comprehensive experimental tests were conducted under various load conditions using a dSpace test bench and a SEMIKRON-based three-phase inverter. The experimental results confirmed the superior stability, performance, and robustness of the proposed control scheme compared to existing control strategies.

REFERENCES

[1] N. Kumar, J. M. Guerrero, D. Kastha, and T. K. Saha, "Power electronics for next-generation drives and energy systems," in *Clean Generation and Power Grids*. Edison, NJ, USA: IET, 2022, pp. 1–240.

[2] T. Liu and X. Wang, "Unified voltage control for grid-forming inverters," *IEEE Trans. Ind. Electron.*, vol. 71, no. 3, pp. 2578–2589, Mar. 2024.
[3] C. Fang, L. Mu, Z. Wang, and G. Chen, "Analysis of grid-forming IIDG's transient-and steady-state fault model," *IEEE Trans. Smart Grid*, vol. 13, no. 2, pp. 1187–1199, Mar. 2022.
[4] T. Liu, X. Wang, F. Liu, K. Xin, and Y. Liu, "Transient stability analysis for grid-forming inverters transitioning from islanded to grid-connected mode," *IEEE Open J. Power Electron.*, vol. 3, pp. 419–432, 2022.
[5] J. Rocabert, A. Luna, F. Blaabjerg, and P. Rodríguez, "Control of power converters in AC microgrids," *IEEE Trans. Power Electron.*, vol. 27, no. 11, pp. 4734–4749, Nov. 2012.
[6] J. Sha, H. Wei, and J. Hu, "Principle, design, and analysis of a novel discrete pulse control for single-phase voltage source inverter," *IEEE Trans. Ind. Electron.*, vol. 71, no. 6, pp. 5693–5703, Jun. 2024.
[7] Y. W. Li, "Control and resonance damping of voltage-source and current-source converters with *LC* filters," *IEEE Trans. Ind. Electron.*, vol. 56, no. 5, pp. 1511–1521, May 2009.
[8] D. G. Holmes, T. A. Lipo, B. P. McGrath, and W. Y. Kong, "Optimized design of stationary frame three phase AC current regulators," *IEEE Trans. Power Electron.*, vol. 24, no. 11, pp. 2417–2426, Nov. 2009.
[9] E. Avci and M. Ucar, "Proportional multi-resonant-based controller design method enhanced with a lead compensator for stand-alone mode three-level three-phase four-leg advanced T-NPC inverter system," *IET Power Electron.*, vol. 13, no. 4, pp. 863–872, Mar. 2020.
[10] M. Benzoubir, N. Gazzam, M. Bougrine, M. Trabelsi, and A. Benalia, "Robust voltage control of autonomous distributed generation system using fractional-order sliding mode control," in *Proc. 49th Annu. Conf. IEEE Ind. Electron. Soc. (IECON)*, Oct. 2023, pp. 1–6.
[11] K. Rayane, A. Rabhi, B. K. Oubbati, and M. Benzoubir, "Enhanced grid-forming inverter control through integral sliding mode control in a cascaded framework," in *Proc. 4th Int. Conf. Smart Grid Renew. Energy (SGRE)*, Jan. 2024, pp. 1–6.
[12] Z. Li, C. Zang, P. Zeng, H. Yu, S. Li, and J. Bian, "Control of a grid-forming inverter based on sliding-mode and mixed H_2/H_∞ control," *IEEE Trans. Ind. Electron.*, vol. 64, no. 5, pp. 3862–3872, May 2017.
[13] J. Li, M. Ali, J. E. Fletcher, and H. I. Nurdin, "Modeling and analysis of multiple inverters with dual-loop-based virtual oscillator control," *IEEE J. Emerg. Sel. Topics Power Electron.*, vol. 10, no. 4, pp. 3963–3974, Aug. 2022.
[14] A. Quedan, W. Wang, D. Ramasubramanian, E. Farantatos, and S. Asgarpoor, "An adaptive virtual oscillator control structure for grid-forming inverters," *IEEE Syst. J.*, vol. 17, no. 3, pp. 3447–3455, 2023.
[15] H. Bakini, N. Mesbahi, M. Kermadi, S. Mekhilef, Y. Zahraoui, M. Mubin, M. Seyedmahmoudian, and A. Stojcevski, "An improved mutated predictive control for two-level voltage source inverter with reduced switching losses," *IEEE Access*, vol. 12, pp. 25797–25808, 2024.
[16] T. Heins, M. Joševski, S. Karthik Gurumurthy, and A. Monti, "Centralized model predictive control for transient frequency control in islanded inverter-based microgrids," *IEEE Trans. Power Syst.*, vol. 38, no. 3, pp. 2641–2652, May 2023.
[17] W. Wu, L. Qiu, X. Liu, J. Ma, J. Rodriguez, and Y. Fang, "Dynamic-linearization-based predictive control of a voltage-source inverter," *IEEE Trans. Ind. Electron.*, vol. 71, no. 4, pp. 3275–3284, Apr. 2024.
[18] J. Rodríguez, R. Heydari, Z. Rafiee, H. A. Young, F. Flores-Bahamonde, and M. Shahparasti, "Model-free predictive current control of a voltage source inverter," *IEEE Access*, vol. 8, pp. 211104–211114, 2020.
[19] J. C. Vasquez, J. M. Guerrero, A. Luna, P. Rodriguez, and R. Teodorescu, "Adaptive droop control applied to voltage-source inverters operating in grid-connected and islanded modes," *IEEE Trans. Ind. Electron.*, vol. 56, no. 10, pp. 4088–4096, Oct. 2009.
[20] R. Bhattarai, N. Gurung, and S. Kamalasadan, "Dual mode control of a three-phase inverter using minimum variance adaptive architecture," *IEEE Trans. Ind. Appl.*, vol. 54, no. 4, pp. 3868–3880, Jul. 2018.
[21] X. Wang, P. C. Loh, and F. Blaabjerg, "Stability analysis and controller synthesis for single-loop voltage-controlled VSIs," *IEEE Trans. Power Electron.*, vol. 32, no. 9, pp. 7394–7404, Sep. 2017.
[22] J. Wang, L. Chen, Z. Liu, Z. Zhang, and X. Zhang, "Optimized parameter design of the dual-loop control for grid-forming VSCs with LC filters," *IEEE Trans. Ind. Appl.*, vol. 58, no. 1, pp. 820–829, Jan. 2022.
[23] A. Akhavan, S. Golestan, J. C. Vasquez, and J. M. Guerrero, "Passivity enhancement of voltage-controlled inverters in grid-connected microgrids considering negative aspects of control delay and grid impedance variations," *IEEE J. Emerg. Sel. Topics Power Electron.*, vol. 9, no. 6, pp. 6637–6649, Dec. 2021.
[24] H. Li, X. Ding, R. Xue, G. Li, and Y. Chen, "Active damping adaptive controller for grid-connected inverter under weak grid," *IEEE Access*, vol. 9, pp. 132442–132454, 2021.
[25] A. Akhavan, J. C. Vasquez, and J. M. Guerrero, "Passivity-based control of single-loop grid-forming inverters," *IEEE J. Emerg. Sel. Topics Ind. Electron.*, vol. 4, no. 2, pp. 571–579, Apr. 2023.
[26] H.-S. Kim, H.-S. Jung, and S.-K. Sul, "Discrete-time voltage controller for voltage source converters with LC filter based on state-space models," *IEEE Trans. Ind. Appl.*, vol. 55, no. 1, pp. 529–540, Jan. 2019.
[27] Z. Zhou, S. Pugliese, and M. Liserre, "Stability enhancement for single-loop voltage controlled voltage-source converters with LC-filter," in *Proc. 47th Annu. Conf. IEEE Ind. Electron. Soc. (IECON)*, Oct. 2021, pp. 1–6.
[28] S. Tolani and P. Sensarma, "Output impedance mitigation at filter resonance for single and three-phase UPS systems with reduced sensor count," in *Proc. 41st Annu. Conf. IEEE Ind. Electron. Soc. (IECON)*, Nov. 2015, pp. 003206–003211.
[29] Y. Geng, Y. Yun, R. Chen, K. Wang, H. Bai, and X. Wu, "Parameters design and optimization for LC-type off-grid inverters with inductor-current feedback active damping," *IEEE Trans. Power Electron.*, vol. 33, no. 1, pp. 703–715, Jan. 2018.
[30] R. Turner, S. Walton, and R. Duke, "Robust high-performance inverter control using discrete direct-design pole placement," *IEEE Trans. Ind. Electron.*, vol. 58, no. 1, pp. 348–357, Jan. 2011.
[31] Z. Li, Y. Li, P. Wang, H. Zhu, C. Liu, and F. Gao, "Single-loop digital control of high-power 400-Hz ground power unit for airplanes," *IEEE Trans. Ind. Electron.*, vol. 57, no. 2, pp. 532–543, Feb. 2010.
[32] J. He, B. Liang, Y. W. Li, and C. Wang, "Simultaneous microgrid voltage and current harmonics compensation using coordinated control of dual-interfacing converters," *IEEE Trans. Power Electron.*, vol. 32, no. 4, pp. 2647–2660, Apr. 2017.
[33] F. D. Freijedo, A. Vidal, A. G. Yepes, J. M. Guerrero, Ó. López, J. Malvar, and J. Doval-Gandoy, "Tuning of synchronous-frame PI current controllers in grid-connected converters operating at a low sampling rate by MIMO root locus," *IEEE Trans. Ind. Electron.*, vol. 62, no. 8, pp. 5006–5017, Aug. 2015.
[34] S. Bacha, I. Munteanu, and A. I. Bratcu, *Power Electronic Converters Modeling and Control*. Springer, 2014.
[35] S. Jafarpour, V. Purba, B. B. Johnson, S. V. Dhople, and F. Bullo, "Singular perturbation and small-signal stability for inverter networks," *IEEE Trans. Control Netw. Syst.*, vol. 9, no. 2, pp. 979–992, Jun. 2022.
[36] Y. Han, A.-T. Jiang, E. A. A. Coelho, and J. M. Guerrero, "Optimal performance design guideline of hybrid reference frame based dual-loop control strategy for stand-alone single-phase inverters," *IEEE Trans. Energy Convers.*, vol. 33, no. 2, pp. 730–740, Jun. 2018.

MOHAMMED E. BENZOUBIR received the Engineer's and master's degrees in automatics from the National Polytechnic School Maurice Audin, Oran, Algeria, in 2020.

Since 2021, he has been a Research Assistant with the Department of Electrical Engineering, University of Amar Telidji. In 2023, he was a Guest Researcher with the Center for Research on Microgrids (CROM) Laboratory, Aalborg University, Denmark, where he furthered his expertise in control strategies for power electronics and microgrids. His research interests include advanced control strategies for power electronics converters, nonlinear control systems, and the integration of renewable energy into microgrids.

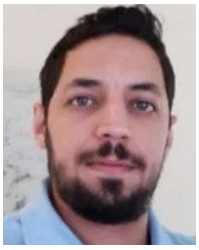

ABDEREZAK LASHAB (Senior Member, IEEE) received the Baccalaureate degree (Hons.) from the High School, Cheikh Ibrahim Bayoud, Constantine, Algeria, in 2007, the bachelor's and master's degrees in electrical engineering from the Université des Frères Mentouri Constantine 1, Constantine, in 2010 and 2012, respectively, and the Ph.D. degree in developing and investigating new converter topologies and control methods of photovoltaic systems with and without storage from the Department of Energy Technology, Aalborg University, Denmark, in 2019.

From 2012 to 2013, he was an Engineer with High Tech Systems (HTS). From 2013 to 2016, he was a Research Assistant with the Université des Frères Mentouri Constantine 1, where he helped teach several electrical engineering courses for undergraduate students. From April 2019 to July 2019, he was a Visiting Researcher with the Chair of Power Electronics, Kiel University, Germany. From 2019 to 2024, he was a Postdoctoral Researcher with Aalborg University. He is currently an Assistant Professor with Aalborg University. His current research interests include power electronics topologies, modeling, and control for photovoltaic systems with and without storage. He serves as a Reviewer for IEEE TRANSACTIONS ON INDUSTRIAL ELECTRONICS, IEEE TRANSACTIONS ON POWER ELECTRONICS, IEEE TRANSACTIONS ON INDUSTRIAL INFORMATICS, IEEE TRANSACTIONS ON SUSTAINABLE ENERGY, *IET Power Electronics*, *IET Electronics Letters*, and several IEEE conferences.

KHALED RAYANE received the bachelor's and master's degrees in electrical engineering from Amar Telidji University of Laghouat, Algeria, in 2014 and 2016, respectively, and the Ph.D. degree in electrical engineering from Amar Telidji University of Laghouat, in 2021. In November 2019, he joined the Department of Electrical and Computer Engineering, Texas A&M University at Qatar, Doha, as a Research Assistant. He is currently an Associate Professor with the Department of Electrical Engineering, Amar Telidji University of Laghouat. His research interests include control systems, smart grids, power electronic converters, and renewable energy sources.

MOHAMMED BENMILOUD (Member, IEEE) received the Ph.D. degree in control engineering, in 2017, under the joint supervision of the University of Amar Telidji, Laghouat, Algeria, and Université Polytechnique Hauts-de-France. Following his Ph.D., he completed a Postdoctoral Fellowship with École Centrale de Nantes, France, from 2017 to 2018, and a Research Associate with the University of Cambridge, U.K., from 2018 to 2019. He is currently an Assistant Professor with the Department of Electronics, University of Amar Telidji. His research interests include advanced control systems, nonlinear dynamics, renewable energy technologies, power electronics, and microgrids.

MOHAMED BOUGRINE received the Engineer's degree in electronics, the master's degree in control systems, and the Ph.D. degree in analysis and control of dynamical systems from the University of Amar Telidji, Laghouat, Algeria, in 2010, 2011, and 2018, respectively. He is currently an Associate Professor with the Department of Electrical Engineering, University of Amar Telidji. His research interests include nonlinear control, hybrid systems, power electronics converters, smart grid, and fuel-cell hybrid vehicles.

ATALLAH BENALIA was born in Algeria, in 1972. He received the B.Sc. degree from the Polytechnic School of Algiers, in 1996, and the Ph.D. degree from Paris-Sud University, France, in 2004. He has been with the University of Amar Telidji, Algeria, as a Full Professor, since 2007, and the Vice Rector of the Scientific Research, since 2015. He currently is with LACoSERE Laboratory, Laghouat University, Algeria. His fields of interest are mainly related to nonlinear control including hybrid systems, sliding mode, and flatness theory, with applications to multilevel converters, renewable energy conversion, active power filters, and fuel cell systems.

MOHAMED TRABELSI (Senior Member, IEEE) received the B.Sc. degree in electrical engineering from INSAT, Tunisia, in 2006, the M.Sc. degree in automated systems, and the Ph.D. degree in energy systems from INSA Lyon, France, in 2006 and 2009, respectively. From October 2009 to August 2018, he has been holding different research positions with Qatar University and Texas A&M University, Qatar. In September 2018, he joined Kuwait College of Science and Technology as an Associate Professor, where he is currently a Full Professor and the Head of the Electronics and Communications Engineering Department. His research interests include control systems with applications arising in the contexts of power electronics, energy conversion, renewable energy integration, and smart grids.

HANI VAHEDI (Senior Member, IEEE) received the Ph.D. degree (Hons.) from École de Technologie Superieure (ÉTS), University of Quebec, Montreal, Canada, in 2016.

After seven years of experience in industry as a power electronics designer and the chief scientific officer, he joined the Delft University of Technology, where he is currently an Assistant Professor with the DCE&S Group, working towards the electrification of industrial processes for clean energy transition. He is also The Technical Lead of Green Village 24/7 Energy Hub, TU Delft, implementing a local microgrid with green energy resources and a hydrogen energy storage system as the future of the energy transition. He has published more than 80 technical papers in IEEE conferences and transactions. He also published a book on Springer Nature and a book chapter in Elsevier. He is the inventor of the PUC5 converter, holds multiple US/world patents, and transferred that technology to the industry, where he developed the first bidirectional electric vehicle DC charger based on his invention. His research interests include multilevel converter topologies, control and modulation techniques, and their applications in the electrification of industrial processes and clean energy transition, such as smart grids, renewable energy conversion, electric vehicle chargers, green hydrogen production (electrolyzers), and fuel-cell systems.

Dr. Vahedi received the Best Ph.D. Thesis Award from ETS, from 2016 to 2017. He is the Co-Chair of the Student and Young Professionals (S&YP) Committee of the IEEE Industrial Electronics Society (IES). He is also an Associate Editor for IEEE TRANSACTIONS ON INDUSTRIAL ELECTRONICS, IEEE OPEN JOURNAL OF INDUSTRIAL ELECTRONICS SOCIETY, and IEEE OPEN JOURNAL OF POWER ELECTRONICS.